JOURNAL OF THERMOPHYSICS AND HEAT TRANSFER
Vol. 15, No. 1, January–March 2001

Inertia and Thermal Convection During Crystal Growth with a Steady Magnetic Field

Nancy Ma*
University of Missouri–Rolla, Rolla, Missouri 65409-0050
and
John S. Walker†
University of Illinois at Urbana–Champaign, Urbana, Illinois 61801

The steady axisymmetric buoyant convection in an electrically conducting liquid in a cylinder with a uniform axial magnetic field is examined. The geometry and boundary conditions are chosen to model the liquid-encapsulated Czochralski growth of compound semiconductor crystals. The objective is to determine the errors associated with the neglect of inertial effects or of convective heat transfer for a series of magnetic field strengths.

Nomenclature

a	=	dimensionless radius of the crystal
B	=	magnetic flux density
b	=	half the dimensionless depth of the melt
c_p	=	specific heat
g	=	9.81 m/s^2
Ha	=	Hartmann number
$\boldsymbol{j}$	=	electric current density
k	=	thermal conductivity
N	=	interaction parameter
Pe	=	Peclet number
p	=	pressure
R	=	inside radius of the crucible
r, θ, z	=	cylindrical coordinates
$\hat{\boldsymbol{r}}, \hat{\boldsymbol{\theta}}, \hat{\boldsymbol{z}}$	=	unit vectors
T	=	dimensionless temperature
U	=	characteristic velocity
$\boldsymbol{v}$	=	dimensionless melt velocity
β	=	volumetric expansion coefficient
μ	=	dynamic viscosity
ρ	=	density
σ	=	electrical conductivity
ϕ	=	electric potential function
ψ	=	Stokes stream function

Introduction

BECAUSE most molten semiconductors have large electrical conductivities, a magnetic field can be used during crystal growth either to control the natural convection with a steady or DC magnetic field or to create a forced convection with a periodic or AC magnetic field. In current crystal-growth applications, the characteristics of AC and DC magnetic fields are very different. AC fields have a frequency of 50 or 60 Hz and a typical magnetic flux density of 5 mT. In this case, 1) the magnetic field, electric current, and electromagnetic body force are decoupled from the flow, which is an ordinary hydrodynamic flow driven by a known body force; and 2) only the time-averaged body force is important. With cylindrical geometries, AC fields are called rotating magnetic fields if they produce an azimuthal body force, and travelling magnetic fields if they produce an axial body force. DC magnetic fields in current applications have strengths from 0.5 to 5.0 T, that is, 100 to 1000 times stronger than AC fields. For such strengths, the flow is a magnetohydrodynamic flow with the electric current intrinsically coupled to the flow. DC magnetic fields are used to eliminate hydrodynamic instabilities leading to deleterious periodic melt motions, and to damp buoyant convections leading to undesirable radial variations of the crystal's composition. This paper is concerned only with DC magnetic fields.

The characteristic velocity for magnetically damped axisymmetric buoyant convection is

$$U = \frac{\rho g \beta (\Delta T)}{\sigma B^2} \tag{1}$$

where ρ, β, and σ are the density, volumetric expansion coefficient, and electrical conductivity of the liquid, respectively, while $g = 9.81$ m/s^2, (ΔT) is the characteristic temperature difference in the liquid, and B is the characteristic magnetic flux density.[1] In the Navier–Stokes equation, the characteristic ratio of the electromagnetic (EM) body-force term to the nonlinear inertial terms is the interaction parameter, $N = \sigma B^2 R/\rho U$, where the radius R of the cylinder containing the liquid is chosen as the characteristic length. With Eq. (1), N varies as B^4. For a strong magnetic field, $N \gg 1$, the EM body force overwhelms inertia, and the nonlinear inertial terms can be dropped from the Navier–Stokes equation. In the energy equation, the characteristic ratio of convective to conductive heat transfer is the Peclet number, $Pe = \rho c_p UR/k$, where c_p and k are the specific heat and thermal conductivity of the liquid. For crystal-growth processes, the volumetric heating from viscous and Joulean dissipation is negligible compared to the heat flux into the melt from external conductive inductive, or radiative heaters.[2] With Eq. (1), Pe varies as B^{-2}. For a strong magnetic field, $Pe \ll 1$ and magnetic damping reduces the melt velocity so much that convective heat transfer is negligible. If inertial effects and convective heat transfer are both negligible, the velocity $\boldsymbol{v}$ and temperature T in the melt are governed by linear equations. With linearity, the solutions for the melt motions due to buoyant convection, thermocapillary convection, crystal and crucible rotations, body forces associated with radio-frequency induction heating, and melt volume depletion can be obtained independently and then superimposed to get the total melt motion.

The goal of modeling the melt motion is to predict important crystal characteristics that depend on the melt motion. One important crystal characteristic is the distribution of additives or dopants, which are added to the melt to give the crystal specific electrical or optical properties. Dopants are either rejected during solidification, leading to higher concentrations in the melt near the crystal–melt interface, or are preferentially absorbed into the crystal, leading to

Received 27 November 1999; revision received 8 May 2000; accepted for publication 17 May 2000.

*Assistant Professor of Mechanical Engineering, Department of Mechanical and Aerospace Engineering and Engineering Mechanics, 1870 Miner Circle.

†Professor of Mechanical Engineering, Department of Mechanical and Industrial Engineering, 1206 West Green Street.

lower concentrations in the melt near the interface. Convective mass transport of dopant-rich or dopant-depleted melt is not negligible, even with very strong magnetic fields, because the diffusion coefficients for dopants in molten semiconductors are very small. A typical ratio of thermal diffusivity to dopant diffusivity is 1000. Even during crystal growth in microgravity, where residual accelerations can be 10,000 times smaller than terrestrial gravity, the convection is large enough to drive significant convective mass transport.[3,4]

In our previous studies[4–8] of dopant transport during the entire period to grow a crystal with several different processes, we have assumed a priori that inertial effects and convective heat transfer are negligible. The purpose of this paper is to determine the errors associated with the neglect of inertial effects and convective heat transfer for various magnetic field strengths and for an important crystal-growth process. We focus on the liquid-encapsulated Czochralski (LEC) process, which is used to grow crystals of compound semiconductors such as gallium arsenide and indium phosphide (InP). In the LEC process, the melt is contained in a cylindrical crucible, and the top surface of the melt is covered with a layer of a liquid encapsulant, which is almost always boron oxide. The encapsulant prevents the escape of the volatile component (i.e., arsenic or phosphorus) and reduces radiative heat losses from the crystal, thus reducing the thermal stresses that produce dislocations in the crystal. Crystal growth starts when a single-crystal seed touches the center of the top surface of the melt. The crystal is allowed to grow to the desired diameter and then lifted upward or "pulled" at a velocity that maintains a constant diameter. In the common bulk-flow approximation, the circular crystal–melt interface and the annular encapsulant–melt interface lie in the same horizontal plane, which moves toward the crucible bottom as the crystal grows.

A uniform axial magnetic field produced by a solenoid around the crystal-growth furnace is generally used for the LEC growth of compound semiconductor crystals.[9–12] Crystals grown in nonuniform axisymmetric magnetic fields were inferior to those grown in a uniform axial magnetic field.[13] To compute the values of the important dimensionless parameters for each magnetic field strength, we use $R = 4.7$ cm (Ref. 9), $(\Delta T) = 20$ K, and the thermophysical properties of molten InP, namely $\rho = 5050$ kg/m^3, $\beta = 4.44 \times 10^{-4}$ K^{-1}, $\sigma = 7.0 \times 10^5$ S/m, $c_p = 424$ J/kg-K, $k = 22.8$ W/m-K, and dynamic viscosity $\mu = 8.19 \times 10^{-4}$ Pa-s. Compound semiconductor crystals are often grown without rotating the crystal or crucible,[9] so we do not include any rotationally driven melt motion. Boron oxide is extremely viscous, so that the buoyant convection velocity in the encapsulant is much smaller than the magnetically damped melt velocity for the magnetic field strengths considered in this paper.[14] Similarly, any variations of the tension of the melt–encapsulant interface are balanced by shear stresses in the encapsulant, with negligible velocities in both liquids, so that there is no thermocapillary convection. Therefore, the melt–encapsulant interface appears to the melt to be a no-slip boundary. If induction heating is used, all the radio-frequency magnetic fields are confined to the graphite susceptor around the crucible, so that induction heating does not produce a melt motion.[15] The solidification rate for compound semiconductors is generally less than 3 μm/s, which is much less than U for the magnetic field strengths considered here. Therefore, we treat only the steady, axisymmetric, buoyant convection in a constant-depth melt. We choose a depth corresponding to a very early stage in the growth of a crystal so that the buoyant convection, inertial effects, and convective heat transfer have their maximum magnitudes. Thus, we compute the largest errors due to neglect of inertial effects and convective heat transfer for each magnetic field strength.

Problem Formulation

In addition to the applied magnetic field produced by the solenoid around the crystal-growth furnace, there is an induced magnetic field that is produced by the electric currents in the melt. The characteristic ratio of the induced to applied magnetic-field strengths is the magnetic Reynolds number, $R_m = \mu_p \sigma U R$, where μ_p is the magnetic permeability of the liquid. For all crystal-growth processes, the value of R_m is extremely small, so that the induced magnetic field is negligible. Because our applied magnetic field is uniform and axial, it is given by $B\hat{\boldsymbol{z}}$, where $\hat{\boldsymbol{r}}, \hat{\theta}, \hat{\boldsymbol{z}}$ are unit vectors for the cylindrical coordinates r, θ, z, with the z axis along the common vertical centerline of the crystal and crucible.

The dimensionless governing equations for a steady, magnetically damped buoyant convection are

$$N^{-1}(\boldsymbol{v}\cdot\nabla)\boldsymbol{v} = -\nabla p + T\hat{\boldsymbol{z}} + \boldsymbol{j}\times\hat{\boldsymbol{z}} + Ha^{-2}\nabla^2\boldsymbol{v} \tag{2a}$$

$$\boldsymbol{j} = -\nabla\phi + \boldsymbol{v}\times\hat{\boldsymbol{z}} \tag{2b}$$

$$\nabla\cdot\boldsymbol{v} = 0 \tag{2c}$$

$$\nabla\cdot\boldsymbol{j} = 0 \tag{2d}$$

$$Pe(\boldsymbol{v}\cdot\nabla)T = \nabla^2 T \tag{2e}$$

Here, $\boldsymbol{v}, \boldsymbol{j}$, and ϕ are the velocity, electric current density, and electric potential function (voltage), normalized by U, σUB, and UBR, respectively; p is the deviation of the pressure from the hydrostatic pressure for the uniform reference density in the Boussinesq approximation, normalized by σUB^2R; T is the deviation of the temperature from the solidification temperature, normalized by (ΔT); and $Ha = BR(\sigma/\mu)^{1/2}$ is the Hartmann number. Equation (2a) is the Navier–Stokes equation, with the buoyant body force $T\hat{\boldsymbol{z}}$ and the EM body force $\boldsymbol{j}\times\hat{\boldsymbol{z}}$ due to the electric current and the applied magnetic field; Eq. (2b) is Ohm's law, with the static electric field $-\nabla\phi$ due to electric charges and the induced electric field $\boldsymbol{v}\times\hat{\boldsymbol{z}}$ due to the melt motion across magnetic field lines; Eqs. (2c) and (2d) guarantee conservation of mass and electric charge; and Eq. (2e) is the energy equation.

For an axisymmetric buoyant convection, all variables are independent of θ, $\boldsymbol{v} = v_r\hat{\boldsymbol{r}} + v_z\hat{\boldsymbol{z}}$, $\boldsymbol{j} = j_\theta\hat{\theta}$, and $\phi = 0$. Ohm's law reduces to $j_\theta = -v_r$, so that $\boldsymbol{j}\times\hat{\boldsymbol{z}} = -v_r\hat{\boldsymbol{r}}$. The uniform axial magnetic field produces an EM body force opposing any radial motion. The EM body force is large, namely σB^2 times the radial velocity, because there are no electrical insulators to block the azimuthal electric current. We introduce a stream function $\psi(r, z)$, so that

$$v_r = \frac{1}{r}\frac{\partial\psi}{\partial z} \tag{3a}$$

$$v_z = -\frac{1}{r}\frac{\partial\psi}{\partial r} \tag{3b}$$

We cross-differentiate the r and z components of Eq. (2a) to eliminate p. The two equations governing ψ and T are

$$N^{-1}\left\{\frac{1}{r}\frac{\partial\psi}{\partial z}\left[\frac{\partial^3\psi}{\partial r^3} - \frac{3}{r}\frac{\partial^2\psi}{\partial r^2} + \frac{3}{r^2}\frac{\partial\psi}{\partial r} + \frac{\partial^3\psi}{\partial r\partial z^2} - \frac{2}{r}\frac{\partial^2\psi}{\partial z^2}\right]\right.$$
$$\left. - \frac{1}{r}\frac{\partial\psi}{\partial r}\left[\frac{\partial^3\psi}{\partial r^2\partial z} - \frac{1}{r}\frac{\partial^2\psi}{\partial r\partial z} + \frac{\partial^3\psi}{\partial z^3}\right]\right\}$$
$$= -r\frac{\partial T}{\partial r} - \frac{\partial^2\psi}{\partial z^2} + Ha^{-2}\left[\frac{\partial^4\psi}{\partial r^4} - \frac{2}{r}\frac{\partial^3\psi}{\partial r^3} + \frac{3}{r^2}\frac{\partial^2\psi}{\partial r^2}\right.$$
$$\left. - \frac{3}{r^3}\frac{\partial\psi}{\partial r} + 2\frac{\partial^4\psi}{\partial r^2\partial z^2} - \frac{2}{r}\frac{\partial^3\psi}{\partial r\partial z^2} + \frac{\partial^4\psi}{\partial z^4}\right] \tag{4a}$$

$$Pe\left[\frac{1}{r}\frac{\partial\psi}{\partial z}\frac{\partial T}{\partial r} - \frac{1}{r}\frac{\partial\psi}{\partial r}\frac{\partial T}{\partial z}\right] = \frac{\partial^2 T}{\partial r^2} + \frac{1}{r}\frac{\partial T}{\partial r} + \frac{\partial^2 T}{\partial z^2} \tag{4b}$$

With R as the characteristic length, the vertical crucible wall lies at $r = 1$. We place the origin in the middle of the melt, so that the crystal–melt and encapsulant–melt interfaces lie at $z = b$, and the crucible bottom lies at $z = -b$, where $2b$ is the dimensionless melt depth. The boundary conditions on ψ are

$$\psi = 0 \tag{5a}$$

$$\frac{\partial \psi}{\partial r} = 0 \qquad \text{at } r = 1 \tag{5b}$$

$$\psi = 0 \tag{5c}$$

$$\frac{\partial \psi}{\partial z} = 0 \qquad \text{at } z = \pm b \tag{5d}$$

The Taylor series for ψ contains only even powers of r, starting with r^2. During the early stages of LEC crystal growth, most of the heat enters the melt from the vertical crucible wall, and so we assume that there is no heat flux through the crucible bottom and that there is a uniform heat flux q through the vertical crucible wall. We choose $(\Delta T) = qR/k$, which implies that $q = 9700$ W/m^2 for our typical InP process. The melt loses heat by conduction and radiation through the semitransparent boron oxide. Because the temperature variation along the melt–encapsulant interface is tiny compared to the temperature variations in the furnace,[16] we assume that the heat flux across the melt–encapsulant interface is uniform. The boundary conditions on T are

$$\frac{\partial T}{\partial r} = 1, \qquad \text{at} \qquad r = 1 \tag{6a}$$

$$\frac{\partial T}{\partial z} = 0, \qquad \text{at} \qquad z = -b \tag{6b}$$

$$T = 0, \qquad \text{at} \qquad z = b, \qquad \text{for} \qquad 0 \le r \le a \tag{6c}$$

$$\frac{\partial T}{\partial z} = -C, \qquad \text{at} \qquad z = b, \qquad \text{for} \qquad a \le r \le 1 \tag{6d}$$

where a is the dimensionless radius of the crystal. The Taylor series for T contains only even powers of r.

Equations (4–6) were solved with a Chebyshev spectral collocation method. A Galerkin method was used for Eqs. (6c) and (6d), instead of the collocation method, to avoid a Gibbs phenomenon associated with the discontinuity in the thermal boundary conditions at $r = a$, $z = b$. For each value of B, we know the values of Ha, N, and Pe for our typical InP process. We begin by computing the inertialess, convectionless solution for the correct value of Ha, $N = \infty$, and $Pe = 0$. As a second step, we add inertial effects by incrementally decreasing N to the correct value with $Pe = 0$. With each decrease of N, we use a continuation method to get the initial guesses of the coefficients in the Chebyshev polynomial representation of ψ, and then we use a Newton–Raphson iterative method to solve the nonlinear equations governing these coefficients.[17] As the final step for each field strength, we add convective heat transfer by incrementally increasing Pe to the correct value. With each increase of Pe, we use the same continuation method to get the initial guesses of the coefficients in the representations of both ψ and T, and the same Newton–Raphson iterative method to solve the coupled nonlinear equations for these coefficients. For each value of B, the numbers of collocation points in the radial and axial directions were increased until the results were independent of these numbers. The required number of collocation points increased as B was increased because the velocity gradients increased near the boundaries. For $B = 0.9$ T, 25 and 29 collocation points in the radial and axial directions, respectively, were sufficient.

Results

We present results for $a = 0.6$ and $b = 0.3$, which correspond to a very early stage in the growth of an InP crystal in our typical LEC process.[9] We have used experimentally measured temperatures to estimate the heat conduction through the boron oxide and measured temperatures throughout the furnace in a simple enclosure model to estimate the radiative heat transfer through the encapsulant. The radiative model includes the spectrally dependent transmissivity of the boron oxide. These models give $C = 0.6$ for an early stage in crystal growth. For our typical InP process, $Ha = 1374.06B$, $N = 10369.6B^4$, and $Pe = 2.773082B^{-2}$, with B in Tesla. The isotherms for $Pe = 0$ are presented in Fig. 1, where $T_{max} = 0.952$. For eight values of B, the maximum values of T and ψ with inertia and convective heat transfer, as well as the values of Ha, N, and Pe, are presented in Table 1.

Table 1 Values of Ha, N, Pe, T_{max}, and ψ_{max} as a function of magnetic flux density

B, T	Ha	N	Pe	T_{max}	ψ_{max}
0.1	137.41	1.037	277.31	0.4352	0.009383
0.2	274.81	16.59	69.327	0.6225	0.0223
0.3	412.22	84.0	30.812	0.7544	0.03293
0.4	549.62	265.5	17.332	0.8212	0.04007
0.5	687.03	648.1	11.092	0.8526	0.0434
0.6	824.44	1343.9	7.703	0.8774	0.04515
0.7	961.84	2489.7	5.659	0.90	0.04579
0.8	1099.3	4247.4	4.333	0.9148	0.04586

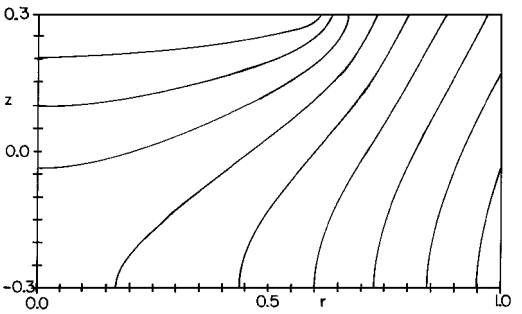

Fig. 1 Isotherms for $Pe = 0$: $T = 0.1$k, for k = 1–9.

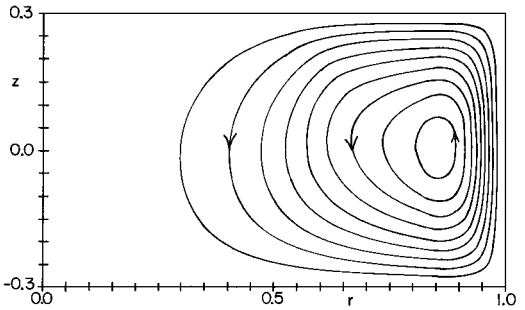

Fig. 2 Streamlines for $Ha = 137.406$, $N = \infty$, and $Pe = 0$: $\psi = 0.004$k, for k = 1–9.

For $B = 0.1$ T, $Ha = 137.406$, $N = 1.037$, and $Pe = 277.3082$. The streamlines for $Ha = 137.406$, $N = \infty$ and $Pe = 0$, are presented in Fig. 2, where $\psi_{max} = 0.03811$. The largest velocity here is $v_z = 0.4$ at $r = 0.95$, $z = 0$. As N is decreased from ∞ to 1.037 for $Ha = 137.406$ and $Pe = 0$, there are three significant changes in the streamlines: 1) with inertial effects augmenting the viscous opposition to the constant buoyant driving force, ψ_{max} decreases by 12.4% to $\psi_{max} = 0.0334$; 2) inertia reduces the large acceleration in the rising flow near the vertical crucible wall, so that the streamlines near $r = 1$ spread out and the location of ψ_{max} moves from $r = 0.86$ to 0.75; and 3) inertia limits the sudden changes in flow direction near $r = 1$ and $z = \pm b$, so that the local streamlines are much more rounded than those in Fig. 2.

The primary effect of increasing Pe with fixed values of Ha and N is that convection carries progressively more of the heat flux from the vertical crucible wall to the crystal–melt and encapsulant–melt interfaces, so that smaller temperature differences are needed for the reduced conductive heat transfer. Thus, the primary effect of increasing Pe is to reduce T_{max} and the average value of $\partial T/\partial r$, thus reducing the buoyant convection. However, when Pe is first increased from zero, the radially inward convection near $z = b$ and the radially outward convection near $z = -b$ make the isotherms more vertical and increase the values of $\partial T/\partial r$ beneath the encapsulant–melt interface. As Pe is increased from zero, T_{max} always decreases, but ψ_{max} first increases because of the more vertical isotherms near

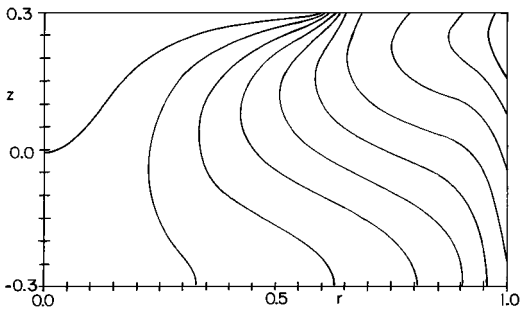

Fig. 3 Isotherms for $Ha = 137.406$, $N = 1.037$, and $Pe = 277.3082$: $T = 0.04k$, for k = 1–10.

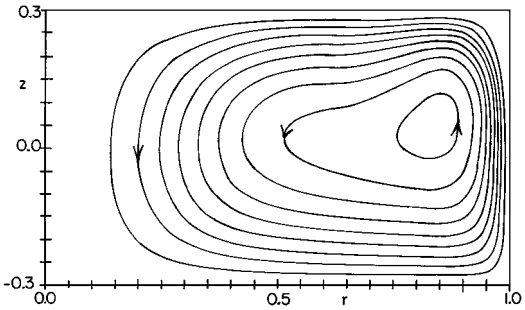

Fig. 4 Streamlines for $Ha = 137.406$, $N = 1.037$ and $Pe = 277.3082$: $\psi = 0.001k$, for k = 1–9.

where ψ_{max} occurs, reaches a maximum at approximately $Pe = 10$, and then decreases with further increases of Pe.

The isotherms for $Ha = 137.406$, $N = 1.037$, and $Pe = 277.3082$ are presented in Fig. 3, where $T_{max} = 0.4352$, which is 54.3% less than T_{max} for $Pe = 0$. Comparison with Fig. 1 shows that convective heat transfer has dramatically changed the shapes of the isotherms as well as reducing the temperatures everywhere. The streamlines for $Ha = 137.406$, $N = 1.037$, and $Pe = 277.3082$ are presented in Fig. 4, where $\psi_{max} = 0.009383$, which is 75.4% less than ψ_{max} for $N = \infty$ and $Pe = 0$. There are three effects of adding convective heat transfer for this magnetic field strength: 1) there is much less melt motion because the radial temperature gradient is much less; 2) convective heat transfer has made the isotherms more vertical beneath the crystal–melt interface, thus increasing $\partial T/\partial r$ here and causing the buoyant convection to extend further toward $r = 0$; and 3) the reduction in the flow has reduced inertial effects so that the location of ψ_{max} has moved back toward $r = 1$ and the sudden changes in flow direction near $r = 1$, $z = \pm b$ have returned. Obviously, it would never be appropriate to neglect either inertial effects or convective heat transfer for this process with $B = 0.1$ T.

For $B = 0.2$ T, $Ha = 274.812$, $N = 16.591$, and $Pe = 69.327$. The only differences between the streamlines for $Ha = 274.812$, $N = \infty$, and $Pe = 0$ and those in Fig. 2 for $B = 0.1$ T are that $\psi_{max} = 0.04094$ and its location is closer to $r = 1$. As a result of these changes, the largest velocity is $v_z = 0.6$ at $r = 0.97$, $z = 0$. In the inertialess, convectionless, asymptotic solution for $Ha \gg 1$ (Ref. 1), 1) the vertically upward flow is confined to a boundary layer that is adjacent to the vertical crucible wall and has an $O(Ha^{-1/2})$ dimensionless thickness; 2) $\psi_{max} \to 0.5b^2 = 0.045$, as $Ha^{-1/2} \to 0$; and 3) the largest velocity is the $O(Ha^{1/2})v_z$ inside the boundary layer at $r = 1$. As N is decreased from ∞ to 16.591 for $Ha = 274.812$ and $Pe = 0$, the only changes in the streamlines are a small shift of the location of ψ_{max} away from $r = 1$ and a slight rounding of the streamlines near $r = 1$, $z = \pm b$. The value of ψ_{max} is reduced by 2.74% to $\psi_{max} = 0.03981$.

As Pe is increased from 0 to 69.327 for $Ha = 274.812$ and $N = 16.591$, the effects of adding convective heat transfer parallel those for $B = 0.1$ T but are much less dramatic. The isotherms indicate significant convection, but are less S-shaped than those in Fig. 3. For example, in Fig. 3, the $T = 0.2$ isotherm starts at $r = 0.91$, $z = -0.3$, goes radially inward to $r = 0.5$, $z = 0.12$, and then goes radially outward to $r = 0.64$, $z = 0.3$, and the $T = 0.2$ isotherm for $B = 0.2$ T starts at $r = 0.56$, $z = -0.3$, goes inward to $r = 0.47$, $z = 0.04$, and then goes outward to $r = 0.64$, $z = 0.3$. As Pe is increased from 0 to 69.327, T_{max} is reduced by 34.6% to 0.6225. The streamlines resemble those in Fig. 4, except that they are less elongated toward $r = 0$, and they are more compressed near $r = 1$ with ψ_{max} closer to $r = 1$, so that there is an upward jet inside the boundary layer on the vertical crucible wall. With inertial effects and convective heat transfer, $\psi_{max} = 0.0223$, which is 45.6% less than that for $N = \infty$ and $Pe = 0$. For $B = 0.2$ T, the error due to neglect of inertial effects is only 2.74%, but the error due to neglect of convective heat transfer is still very large.

For $B = 0.3$ T, $Ha = 412.217$, $N = 83.997$, and $Pe = 30.812$. The only differences between the streamlines for $Ha = 412.217$, $N = \infty$, and $Pe = 0$ and those in Fig. 2 are that $\psi_{max} = 0.04202$ and its location moves closer to $r = 1$, so that the maximum velocity is $v_z = 0.8$ at $r = 0.975$, $z = 0$. When N is decreased from ∞ to 83.997 for $Ha = 412.217$ and $Pe = 0$, there is no perceptible change in the streamlines and the change in ψ_{max} is less than 0.1%. As Pe is increased from 0 to 30.812 for $Ha = 412.217$ and $N = 83.997$, T_{max} decreases by 20.8% to 0.7544 and ψ_{max} decreases by 21.6% to 0.03293. With convective heat transfer, 1) T_{max} occurs at $z = 0.22$ as a result of the strong upward flow near $r = 1$, 2) the isotherms are nearly vertical for $r > 0.5$, and 3) the isotherms for $r < 0.5$ more closely resemble those in Fig. 1 than those in Fig. 3. The streamlines with convective heat transfer closely resemble those for $Pe = 0$ with only slight elongation toward $r = 0$. For $B = 0.3$ T, inertial effects are truly negligible, but there is still a large error in the neglect of convective heat transfer.

For $B = 0.4$ T, $Ha = 549.623$, $N = 265.46$, and $Pe = 17.332$. For $N = \infty$ and $Pe = 0$, $\psi_{max} = 0.04289$. Again, the change with the addition of inertial effects is less than 0.1%. With the addition of convective heat transfer, T_{max} is reduced by 13.7% to 0.8212 and ψ_{max} is reduced by 6.6% to 0.04007. The differences between the shapes of the streamlines with and without convective heat transfer are small, namely only a very small elongation of some streamlines toward $r = 0$ and a very slight shift of the streamlines near $r = 1$ where the largest velocity occurs. For the isotherms, the vertical crucible wall is nearly isothermal and the other isotherms are approaching those in Fig. 1.

For $B = 0.5$ T, $Ha = 687.029$, $N = 648.1$, and $Pe = 11.092$. Inertial effects are totally negligible. Without convective heat transfer, $\psi_{max} = 0.04295$, and with convective heat transfer, $\psi_{max} = 0.0434$. For $Pe = 11.092$, the increase of ψ_{max} because the isotherms become more vertical is larger than the decrease of ψ_{max} because the temperatures decrease as convection carries part of the heat flux. Convective heat transfer still decreases T_{max} by 10.4% to 0.8526, but the change in ψ_{max} is only 1.0%.

For $B = 0.6$ T, $Ha = 824.435$, $N = 1343.9$, and $Pe = 7.703$. Without convective heat transfer, $\psi_{max} = 0.04371$, and with convective heat transfer, $\psi_{max} = 0.04515$, a 3.2% increase. Convective heat transfer reduces T_{max} by 7.8% to 0.8774. For $B = 0.7$ T, $Ha = 961.84$, $N = 2489.7$, and $Pe = 5.659$. Without convective heat transfer, $\psi_{max} = 0.04406$, and with convective heat transfer, $\psi_{max} = 0.04579$, a 3.8% increase. T_{max} is reduced by 5.5% to 0.9. For $B = 0.8$ T, $Ha = 1099.25$, $N = 4247.4$, and $Pe = 4.333$. Without convective heat transfer, $\psi_{max} = 0.04416$, and with convective heat transfer, $\psi_{max} = 0.04586$, a 3.7% increase. Therefore, the increase of ψ_{max} due to convective heat transfer reaches a maximum of less than 4% around $B = 0.7$ T and then decreases with further increases in B. For $B = 0.8$ T, convective heat transfer reduces T_{max} by 3.9% to 0.9148.

Three different values of ψ_{max} are plotted for $0.1 \text{ T} \le B \le 0.9$ T in Fig. 5. For all three curves, $Ha = 1374.06B$. For curve 1, $N = \infty$ and $Pe = 0$; for curve 2, $N = 10369.6B^4$ and $Pe = 0$; and for curve 3, $N = 10369.6B^4$ and $Pe = 2.773082B^{-2}$. As noted earlier, the error due to the neglect of inertial effects is only 2.7% for $B = 0.2$ T and is truly negligible for $B \ge 0.3$ T. Because effects of more vertical isotherms and of reduced temperatures partially cancel for $Pe < 15$, the error in the solution for the melt motion due to the neglect of convective heat transfer is less than 4% for $B > 0.43$ T. The values

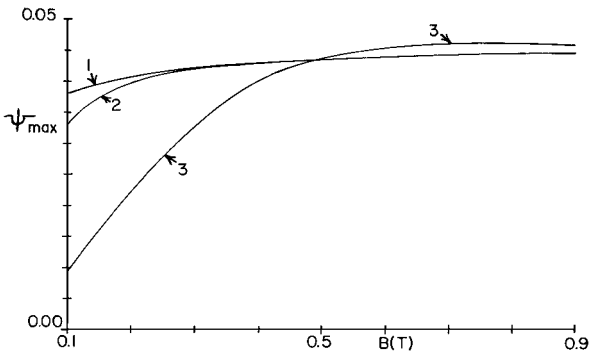

Fig. 5 Maximum value of the stream function vs magnetic field strength: actual *Ha* for all three curves, $N = \infty$ and $Pe = 0$ for curve 1, actual N and $Pe = 0$ for curve 2, and actual N and actual Pe for curve 3.

of ψ_{max} with and without convective heat transfer are approaching the asymptotic value of 0.045 from above and below, respectively, as B is increased.

Conclusions

We have determined the errors associated with the neglect of inertial effects or of convective heat transfer for a dimensionless melt depth of 0.6, corresponding to a very early stage in the growth of an InP crystal by the LEC process.[9] As the melt volume is depleted by solidification, ψ_{max} varies roughly as b^2, so that the effects of inertia and convective heat transfer decrease rapidly. Therefore, we have computed the maximum errors for this process for each magnetic field strength. The same type of study could be done for other processes and other materials. Probably most such situations have comparable errors. The notable exception is the Czochralski growth of silicon crystals, because crystals 30 cm in diameter are currently being grown commercially. With the much greater radius and melt depth, much stronger magnetic fields would be needed to make the effects of inertia and of convective heat transfer small.

Acknowledgments

This research was supported by NASA under Grants NAG8-1656 and NAG8-1453 and by the University of Missouri Research Board. The calculations were performed on a workstation donated by the International Business Machines Corporation.

References

[1]Hjellming, L. N., and Walker, J. S., "Melt Motion in a Czochralski Crystal Puller with an Axial Magnetic Field: Motion Due to Buoyancy and Thermocapillarity," *Journal of Fluid Mechanics*, Vol. 182, 1987, pp. 335–368.

[2]Langlois, W. E., and Lee, K. J., "Czochralski Crystal Growth with an Axial Magnetic Field: Effects of Joulean Heating," *Journal of Crystal Growth*, Vol. 62, No. 3, 1983, pp. 481–486.

[3]Ma, N., and Walker, J. S., "Magnetic Damping of Buoyant Convection During Semiconductor Crystal Growth with G-Jitters," *Journal of Thermophysics and Heat Transfer*, Vol. 11, No. 2, 1997, pp. 212–215.

[4]Ma, N., and Walker, J. S., "Segregation During Bridgman Crystal Growth in Space with an Axial Magnetic Field," *Magnetohydrodynamics*, Vol. 35, No. 2, 1999, pp. 155–159.

[5]Ma, N., and Walker, J. S., "Dopant Transport During Semiconductor Crystal Growth with Magnetically Damped Buoyant Convection," *Journal of Crystal Growth*, Vol. 172, Nos. 1/2, 1997, pp. 124–135.

[6]Ma, N., and Walker, J. S., "Validation of Strong Magnetic Field Asymptotic Models for Dopant Transport During Semiconductor Crystal Growth," *Journal of Crystal Growth*, Vol. 180, Nos. 3/4, 1997, pp. 401–409.

[7]Ma, N., and Walker, J. S., "A Model of Dopant Transport During Bridgman Crystal Growth with Magnetically Damped Buoyant Convection," *Journal of Heat Transfer*, Vol. 122, No. 1, 2000, pp. 159–164.

[8]Ma, N., and Walker, J. S., "A Parametric Study of Segregation Effects During Vertical Bridgman Crystal Growth with an Axial Magnetic Field," *Journal of Crystal Growth*, Vol. 208, Nos. 1–4, 2000, pp. 757–771.

[9]Bliss, D. F., Hilton, R. M., and Adamski, J. A., "MLEK Crystal Growth of Large Diameter (100) Indium Phosphide," *Journal of Crystal Growth*, Vol. 128, Nos. 3/4, 1993, pp. 451–456.

[10]Carlson, D. J., and Witt, A. F., "Quantitative Analysis of the Effects of Vertical Magnetic Fields on Microsegregation in Te-Doped LEC GaAs," *Journal of Crystal Growth*, Vol. 116, Nos. 3/4, 1992, pp. 461–472.

[11]Kimura, T., Katsumata, T., Nakajima, M., and Fukuda, T., "The Effect of Strong Magnetic Field on Homogeneity of LEC GaAs Single Crystal," *Journal of Crystal Growth*, Vol. 79, Nos. 1–3, 1986, pp. 264–270.

[12]Miyairi, H., Inada, T., Eguchi, M., and Fukuda, T., "Growth and Properties of InP Single Crystals Grown by the Magnetic Field Applied LEC Method," *Journal of Crystal Growth*, Vol. 79, Nos. 1–3, 1986, pp. 291–295.

[13]Bryant, G. G., Bliss, D. F., Leahy, D., Lancto, R., Ma, N., and Walker, J. S., "Crystal Growth of Bulk InP from Magnetically Stabilized Melts with a Cusped Field," *International Conference on Indium Phosphide and Related Materials*, Inst. of Electrical and Electronics Engineers, Piscataway, NJ, 1997, pp. 416–419.

[14]Hjellming, L. N., and Walker, J. S., "Isothermal Melt Motion in a Liquid-Encapsulated Czochralski Crystal Puller with an Axial Magnetic Field," *Physico-Chemical Hydrodynamics*, Vol. 10, No. 1, 1988, pp. 107–131.

[15]Ma, N., Bliss, D. F., Anselmo, A. P., and Walker, J. S., "Radio-Frequency Induction Heating for Semiconductor Crystal Growth from a Crucible," *ASME Proceedings of the 31st National Heat Transfer Conference*, edited by V. Prasad, T. L. Bergman, S. T. Thynell, Y. Joshi, D. A. Zumbrunnen, P. J. Prescott, C. L. Chan, U. Chandra, S. Kumar, Z. Xu, S. E. Gianoulakis, C. Clarksean, and S. H. K. Lee, Vol. HTD-323, American Society of Mechanical Engineers, New York, 1996, pp. 306–313.

[16]Prasad, V., Bliss, D. F., and Adamski, J. A., "Thermal Characterization of the High Pressure Crystal Growth System for In-Situ Synthesis and Growth of InP Crystals," *Journal of Crystal Growth*, Vol. 142, Nos. 1/2, 1994, pp. 21–30.

[17]Lentini, M., and Keller, H. B., "The Von Karman Swirling Flow," *SIAM Journal on Applied Mathematics*, Vol. 38, No. 1, 1980, pp. 52–64.